Supplementary Information: Majorana modes with side features in magnet-superconductor hybrid systems

Daniel Crawford,[1] Eric Mascot,[2] Makoto Shimizu,[3] Philip Beck,[4] Jens Wiebe,[4] Roland Wiesendanger,[4] Harald O. Jeschke,[5] Dirk K. Morr,[2] and Stephan Rachel[1]

[1] *School of Physics, University of Melbourne, Parkville, VIC 3010, Australia*
[2] *Department of Physics, University of Illinois at Chicago, Chicago, IL 60607, USA*
[3] *Department of Physics, Okayama University, Okayama 700-8530, Japan*
[4] *Department of Physics, University of Hamburg, D-20355 Hamburg, Germany*
[5] *Research Institute for Interdisciplinary Science, Okayama University, Okayama 700-8530, Japan*

SUPPLEMENTARY NOTE 1. DENSITY FUNCTIONAL THEORY CALCULATIONS

In the main text, the orbital-resolved electronic density of states (DOS) of the d-orbitals of the Mn atoms is shown in Fig. 1 c and e. Here we also show the total electronic DOS in Supplementary Fig. 1, separated into spin-up (blue) and spin-down (red) components. The previously presented Mn d-orbitals are shown as black thick lines (increased by a factor 5 for clarity). The black thin horizontal line marks the Fermi energy.

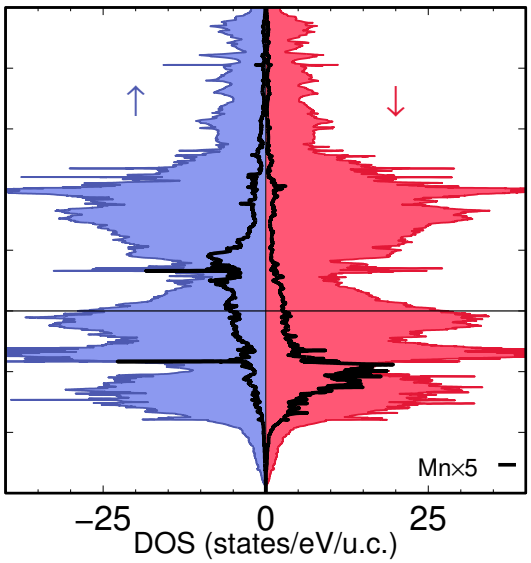

Supplementary Figure 1. **Electronic DOS for the supercell with $d_{\mathrm{Mn-Mn}} = 3.3$Å chains on Nb(110).** The calculation is performed with generalized gradient approximation and spin-orbit coupling (GGA+SO) with ferromagnetically aligned magnetic moments of Mn and quantization axis c, representing the DFT ground state of the system. Blue and red DOS stand for spin minority (up arrow) and majority (down arrow), respectively. The Mn DOS is shown by black lines and multiplied by 5 for clarity.

SUPPLEMENTARY NOTE 2. 40-BAND TIGHT BINDING AND SUPERCONDUCTING 80-BAND MODELS

The projected 40-band tight-binding model describes the d-orbitals of four atoms per unit cell; one atom is on top (the "Mn atom", shown in purple in Fig. 1a of the main text) and three underneath, one in the center and one on both sides (the "Nb atoms", shown in yellow in Fig. 1a of the main text). The model contains complex hoppings up to fifth neighbors being spin-imbalanced due to the spin polarization. The 40-band model contains extra hoppings in the y direction stemming from the original DFT-based model. We remove these hoppings to work in a purely-1D system. We justify this by inspecting the 2D spectra (Supplementary Fig. 2). The flat bands in the k_y direction indicate the absence of any dispersion, thus allowing us to treat the model as one-dimensional and to dismiss any hoppings in the y-direction.

In the following, we focus on the superconducting 80-band model (see Methods in the main text). As mentioned in the main text, the peculiar side features appear only for certain values of Δ, since different orbital contributions are sensitive to the choice of Δ. In Sup-

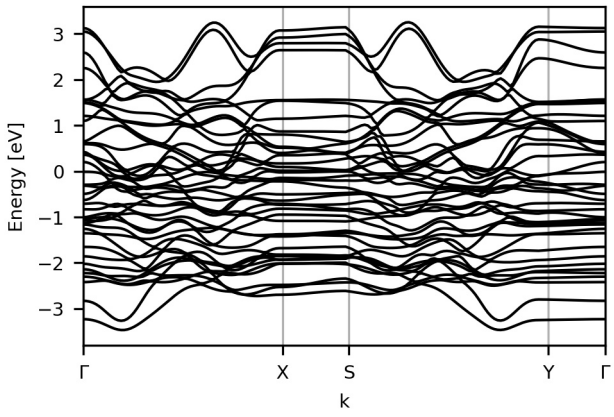

Supplementary Figure 2. **Normal state band structure of 40-band model.** We observe flat bands at low energies when varying k_y, *i.e.*, between X and S and between Y and Γ. A purely 1D model with $\boldsymbol{k} = (k_x, 0)$ is thus justified.

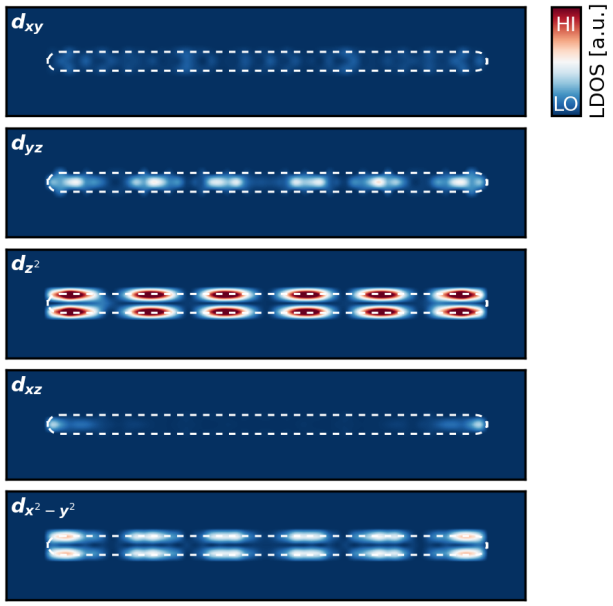

Supplementary Figure 3. **Orbital-resolved real-space LDOS plots at zero energy.** The data shown here is the same as in Fig. 2 c of the main text (for Mn_{52}, $\Delta = 270\,\mathrm{meV}$), but resolved by the contributions of the five Mn d orbitals. Theoretical LDOS is always evaluated in the plane of the chain.

plementary Fig. 3 we show the orbital-resolved version of the zero-energy LDOS (always evaluated in the plane of the chain) presented in Fig. 2 c of the main text (Mn_{52}, $\Delta = 270\,\mathrm{meV}$). The manganese d_{z^2} orbital dominates the LDOS contribution, but also the $d_{x^2-y^2}$ orbital has the same characteristic structure, albeit with weaker intensity. In contrast, the d_{xz} orbital supports localized states at the chain ends only, and the d_{yz} orbital reveals a periodic intensity, but in the center of the chain and not on the sides. Low-energy LDOS plots for other values of Δ appear to have the same structure as one of the other orbitals or a combination of multiple orbitals. That is, MZMs can be localized in the center of the chain, can be oscillatory in the center, or appear as side features. The LDOS plots with side features shown in Fig. 2 c of the main text are only one particular type of MZMs present in the topologically non-trivial range of Δ.

In Fig. 2 of the main text we displayed chain lengths matching the experimental systems. Numerically, we can explore arbitrary chain lengths (up to computational limits). Some examples are shown for chains with $N = 128$ sites in Supplementary Fig. 4; the figure is analogous to Fig. 2 from the main text. We find cases where the MZMs are strongly localized at the ends of the chain; cases where the MZMs are localized at the ends but pushed to the side of the chain; and cases where side features oscillate.

We compute all coherence lengths $v_F/\Delta_{\mathrm{gap}}$ (stemming from multiple bands) and compute the average coherence length. In Supplementary Fig. 5 we show average, smallest and largest coherence lengths as a function of Δ, extracted from the band structure of the 40-band tight-binding model. In the following, we concentrate on the average coherence length only. In general, coherence lengths are long and we expect strong hybridization effects of MZMs. Only for relatively long chains (> 100 sites) and for large Δ (> 150 meV) do well-localized end states appear.

SUPPLEMENTARY NOTE 3. SIMPLIFIED SINGLE-ORBITAL MODEL

We give here the formal definition of the simplified model introduced in the main text, in technical detail. We then present some extra results: phase diagrams, spectra, and a discussion on coherence lengths in this model. Finally, we present a modified version of the model where we have extended the substrate around the magnetic chain.

A. Definition

We start with the standard Shiba chain model [1], and extend to a four atom unit cell. The operators $c_x^{(i)} = (c_{x,\uparrow}^{(i)}, c_{x,\downarrow}^{(i)})$ annihilate an atom of type $i = 0, 1, 2, 3$ on site x; $i = 0$ refers to the magnetic adatom, $i = 1$ to the substrate Nb atom in the centre, and $i = 2, 3$ to the Nb substrate atoms on either side of the adatoms. The Hamiltonian is

$$H = H_t + H_\mu + H_\alpha + H_\Delta + H_J. \tag{1}$$

H_t is the hopping Hamiltonian. In the general case, hopping amplitudes t_{ij} are defined in Supplementary Fig. 6.

$$H_t = \sum_{i,j,x} (t_{ij} c_x^{(i)\dagger} c_x^{(j)} + t_{ij} c_x^{(i)\dagger} c_{x+1}^{(j)} + \mathrm{H.c.}). \tag{2}$$

with $i, j \in [0, 1, 2, 3]$. The first term describes hopping within the unit cell (thus $i \neq j$), and the second term between neighboring unit cells. H_μ is the chemical potential,

$$H_\mu = \sum_{i,x} -\mu c_x^{(i)\dagger} c_x^{(i)} \ . \tag{3}$$

H_α is Rashba spin-orbit coupling. In the general case, Rashba amplitudes are defined by a matrix $\alpha_{ij}(x, x{+}1) = \alpha_{ij}$. All hoppings are associated with $i\alpha\sigma_y$ with α being the Rashba amplitude.

$$H_\alpha = \sum_{i,j,x} (i\alpha_{ij} c_x^{(i)\dagger} \sigma_2 c_x^{(j)} + i\alpha_{ij} c_x^{(i)\dagger} \sigma_2 c_{x+1}^{(j)} + H.c.) \ . \tag{4}$$

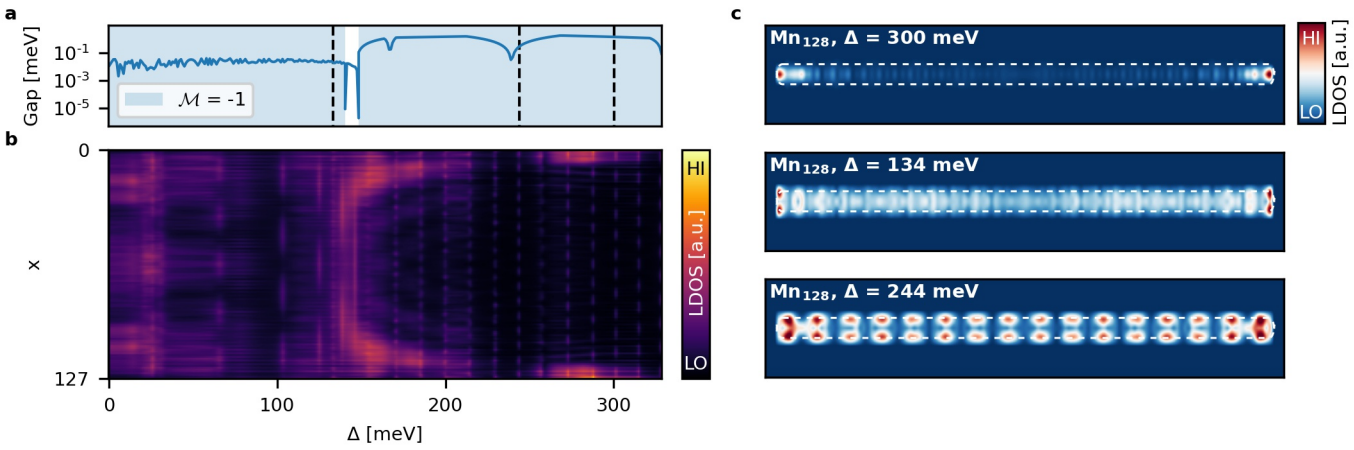

Supplementary Figure 4. **Analysis of DFT-based superconducting 80-band model for $N = 128$. a,** Topological phase diagram as a function of the bare superconducting amplitude Δ (topological region in blue with $\mathcal{M} = -1$, and white is trivial). The gap size is shown as the blue curve. **b,** LDOS as a function of lattice site along x and Δ (the y-dependence has been summed up such that LDOS appears one-dimensional). **c,** Examples of zero-energy LDOS(x,y) for various values of Δ, as indicated by the dashed vertical lines in a, with pronounced side features. Chain length $N = 128$, the value of Δ is given within the panels.

H_Δ represents s-wave onsite superconductivity, and is restricted to the substrate sites $i \in [1, 2, 3]$,

$$H_\Delta = \Delta \sum_{i,x} c^{(i)\dagger}_{x,\uparrow} c^{(i)\dagger}_{x,\downarrow} + \text{H.c.} \tag{5}$$

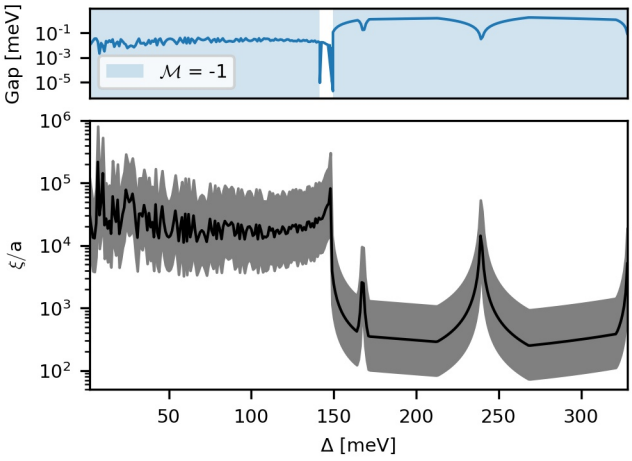

Supplementary Figure 5. **Spectral gap, topological invariant and coherence length of the superconducting 80-band model.** (Top) Spectral gap and topological invariant, identical to Fig. 2 a of the main text. (Bottom) Coherence length $\xi = v_F/\Delta_{\text{gap}}$ for the superconducting 80-band model; a is the lattice spacing. Due to the multi-orbital character of the model, we observed several band crossings at the Fermi energy. The black line corresponds to the average coherence length; the range between minimum and maximum coherence lengths are indicated by the shaded region. For small values of Δ much longer chains are required to avoid strong hybridization effects than for large values of Δ.

H_J is the ferromagnetically aligned Zeeman field, and is restricted to the adatoms $i = 0$,

$$H_J = J \sum_x c^{(0)\dagger}_x \sigma_3 c^{(0)}_x. \tag{6}$$

By choosing different combinations of hoppings (both spin-preserving, *i.e.*, t_{ij}, and spin-flip hoppings, *i.e.*, α_{ij}) we have generated several variants of Eq. (1); all these models generically show side features.

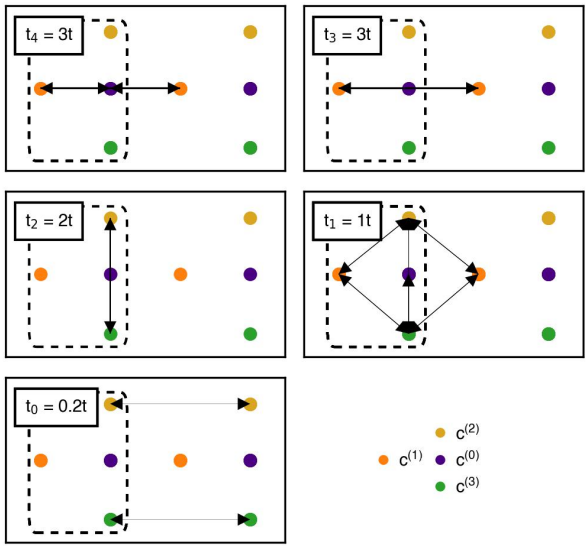

Supplementary Figure 6. **Illustration of all hopping processes in the single-orbital model Eq. (1).** Arrow thickness indicates the real hopping amplitudes between the indicated atoms, defining Eq. (2). The dashed rectangle indicates the unit cell.

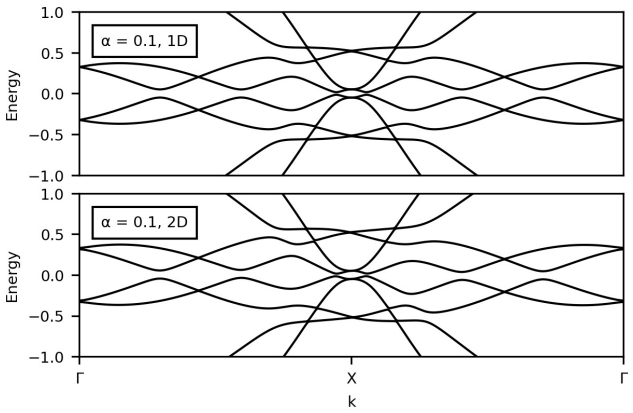

Supplementary Figure 7. **Comparison of Rashba Hamiltonian convention for large Rashba SOC**. Superconducting spectra for 1D-Rashba choice (top) and 2D-Rashba choice (bottom) for $\alpha = 0.1t$.

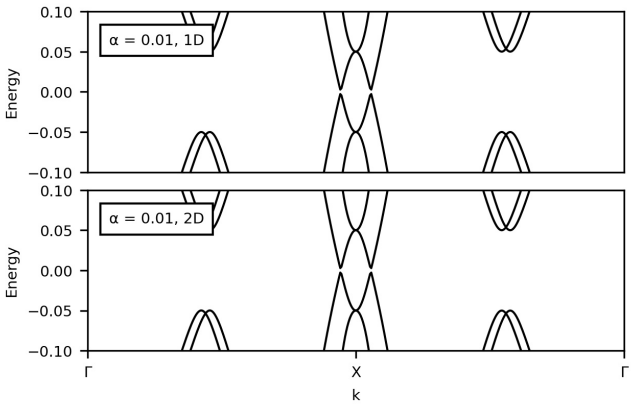

Supplementary Figure 8. **Comparison of Rashba Hamiltonian convention for small Rashba SOC.** Superconducting spectra for 1D-Rashba choice (top) and 2D-Rashba choice (bottom) for $\alpha = 0.01t$.

In the following, we focus on a particular version of Eq. (1) with the hoppings defined in Supplementary Fig. 6; Rashba spin-orbit coupling lies exclusively along the same arrows.

1. 1D-Rashba vs. 2D-Rashba SOC

Because the unit cell of our 1D model is 2D, *i.e.*, has spatial dependence in both x and y directions, the definition of Rashba spin-orbit coupling is ambiguous. We could choose $i\alpha\sigma_x$ in y direction, $i\alpha\sigma_y$ in x direction, and a combination for diagonal hoppings (2D choice). Alternatively, we could uniformly choose $i\alpha\sigma_y$ in all directions, and fix the sign convention of "+" for $+y$ and "−" for $-y$ (1D choice).

For the 2D choice the Rashba part of the Hamiltonian is given by

$$\begin{aligned} H_\alpha = &\sum_{i,j\in\{0,1\},x} (i\alpha_{ij} c_x^{(i)\dagger}\sigma_2 c_x^{(j)} + i\alpha_{ij} c_x^{(i)\dagger}\sigma_2 c_{x+1}^{(j)}) \\ &+ \sum_{i=1,j\in\{2,3\},x} (i\alpha_{ij} c_x^{(i)\dagger}\sigma_1 c_x^{(j)} + i\alpha_{ij} c_x^{(i)\dagger}\sigma_2 c_x^{(j)}) \\ &+ \sum_{i\in\{0,1\},j\in\{2,3\},x} (i\alpha_{ij} c_x^{(i)\dagger}\sigma_1 c_x^{(j)} + i\alpha_{ij} c_x^{(i)\dagger}\sigma_2 c_{x+1}^{(j)}) \\ &+ \sum_{i,j\in\{0,2,3\},x} (i\alpha_{ij} c_x^{(i)\dagger}\sigma_1 c_x^{(j)}) + \text{H.c.} \end{aligned} \tag{7}$$

Hoppings in the x direction are associated with σ_2, in the y direction with σ_1, and along diagonals $\pm x \pm y$ with $\pm i\sigma_1 \pm i\sigma_2$.

We compare superconducting spectra under the two different implementations of Rashba SOC (Supplementary Fig. 7 and Supplementary Fig. 8) and find the spectra are almost identical. Hence, the choice does not matter. Also the eigenstates are similar. In order to keep the model as simple as possible, we chose the 1D-Rashba convention in the main text.

B. Methods

To quantify the presence of side features, we define a simple quantity, the *side feature weight* (SFW), specifically for states closest to $E = 0$. Consider the $E = 0$ LDOS,

$$\rho_x^{(i)} = \text{LDOS}(c_x^{(i)}) \ . \tag{8}$$

We then define the side feature weight of the state $|\psi\rangle$,

$$S(|\psi\rangle) = \frac{\sum_x^L \rho_x^{(2)}}{\sum_x^L \rho_x^{(0)} + \sum_x^L \rho_x^{(1)} + \sum_x^L \rho_x^{(2)}}. \tag{9}$$

Here we sum over the spatial position x from 0 to chain length $L-1$ (unless otherwise specified $L = 51$ sites). Typically we present side feature weight as a function of the free parameters μ and J, with fixed Δ and α. For easy reading we multiply the side feature weight by the topological index, $+1$ (-1) corresponding to the topologically trivial (non-trivial) phase. Negative side feature weights correspond to the topologically superconducting regime, *i.e.*, the zero-energy state represents a MZM with side features. The side feature weight is shown in the phase diagrams of the following subsection.

C. Phase diagrams

We present a representative phase diagram in Fig. 3 c of the main text. It turns out that the specific parameters chosen are not too important: as long as the gap is small

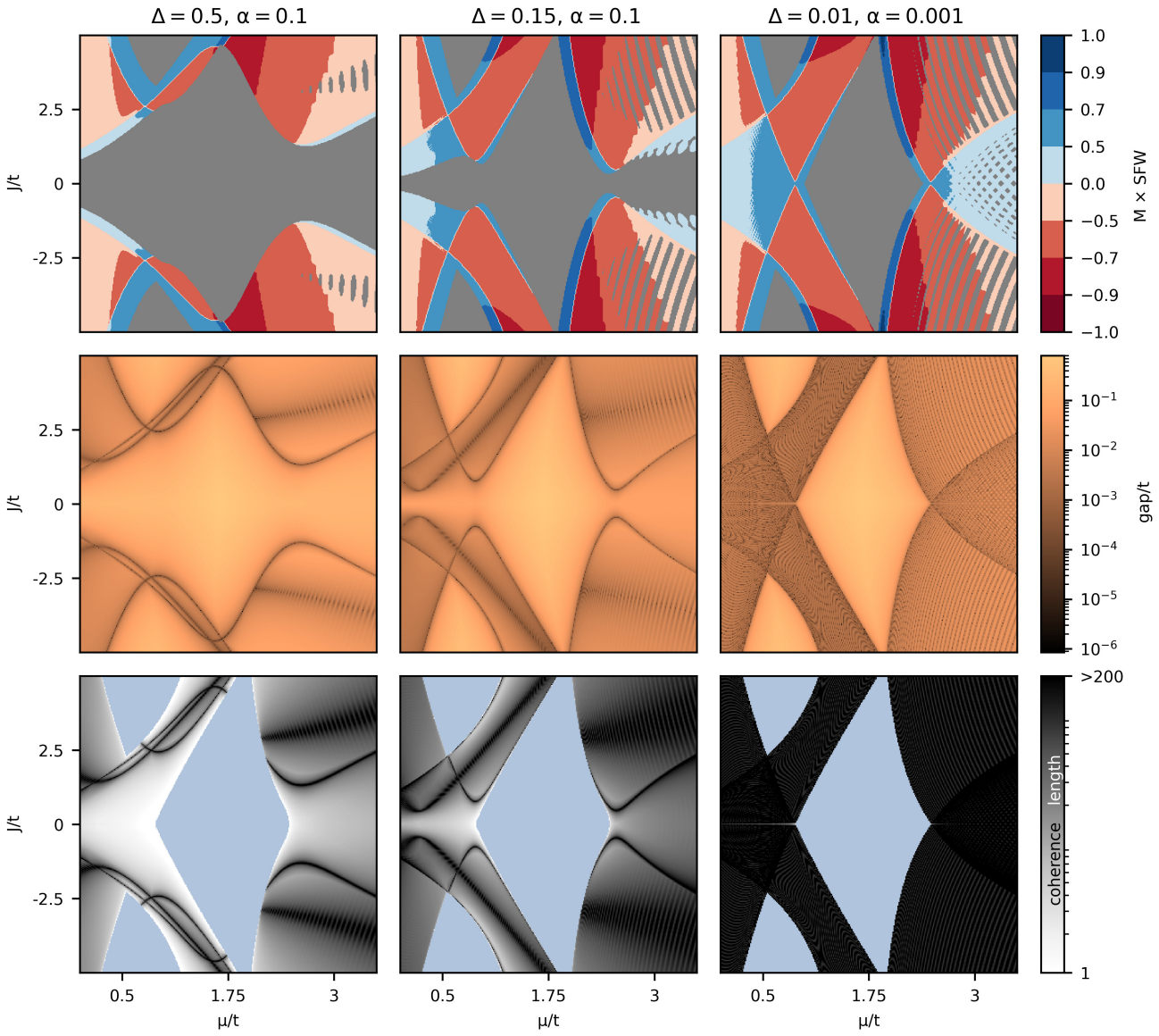

Supplementary Figure 9. **Topological phase diagram, side-feature weight, gap size and coherence length.** All panels correspond to model (1) with Δ and α as specified above the top panels for the entire column, and are shown as a function of J/t and μ/t. The first column corresponds to the largest, and the third to the smallest gap sizes. **First row:** Topological invariant M multiplied by side feature weight $S(|\psi\rangle)$, where $|\psi\rangle$ is the state with energy closest to $E = 0$. Red (blue) regions are topologically nontrivial (trivial). Strong intensities indicate large side feature weights. Note that a small gap is required to reach high side feature weights. Grey regions correspond to lowest energy states with $E > 0.04\,t$, which are thus not of interest. **Second row:** Gap diagrams. Note that the gap closing lines can correspond to phase transitions in the first row. Small gap sizes ($10^{-2}t \ldots 10^{-5}t$) are associated with large side feature weight. **Third row:** Coherence length $\xi = v_F/\Delta_{\text{gap}}$ of the corresponding low-energy state. Light blue regions have insulating normal state, thus the coherence length is ill-defined. Note that ξ can be significantly larger than 200 sites. System size for all panels is $N = 51$.

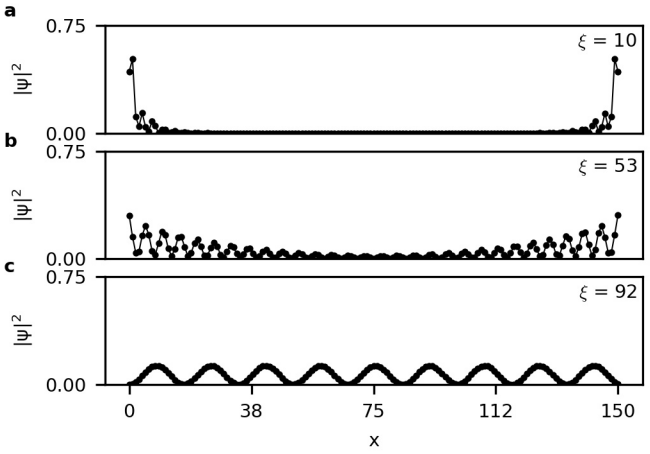

Supplementary Figure 10. **Examples of wavefunctions $|\psi|^2$ with different coherence lengths.** Shown is $|\psi|^2$ of model (1), summed over atoms and spin, lowest-energy state for OBC in the topological regime, thus corresponding to (hybridized) MZMs. The coherence length ξ is shown in each figure panel. **a,** Large gap regime; parameters used $(\Delta, \alpha, \mu, J) = (0.15, 0.1, 1.35, 6)t$. **b,** Medium gap regime; parameters used $(\Delta, \alpha, \mu, J) = (0.15, 0.1, 2.4, 4)t$. **c,** Small gap regime; parameters used $(\Delta, \alpha, \mu, J) = (0.01, 0.05, -2, 4)t$. Smaller gaps are associated with longer coherence lengths and so the MZMs hybridize and oscillate in the chain bulk.

we can find side features. We show phase diagrams and gap diagrams for several parameters in the first and second row of Supplementary Fig. 9, where different columns correspond to large, medium and small gap sizes. For "large gaps" (left column) 65% of the entire phase diagram shows notable side features (SFW > 0.5), and about 9% of the topological region displays significant side features (SFW > 0.7). For "medium gaps" (middle column) 75% of the entire phase diagram shows notable side features (SFW > 0.5), and about 11% of the topological region displays significant side features (SFW > 0.7). For "small gaps" (right column) about 75% of the entire phase diagram shows notable side features (SFW > 0.5), and about 15% of the topological region displays significant side features (SFW > 0.7). Of course the topological phase is the same for all chain lengths and it is, hence, sufficient to show one case ($N = 51$). We note that the side-feature weight is clearly chain-length dependent.

D. Coherence length

As with the 80-band model we compute the approximate coherence length $\xi \sim v_F/\Delta_{\text{gap}}$ (Supplementary Fig. 9, third row) for the simplified model (1) where Δ_{gap} is the effective gap size shown in the second row of Supplementary Fig. 9. Due to the small gap sizes, some of the coherence lengths are as large as 10 000 or even 100 000 sites. As a consequence, hybridization effects can be drastic. We can readily see this in the zero-energy wavefunctions for open boundary conditions (OBC); examples are presented in Supplementary Fig. 10 for $N = 151$ where for decreasing gap size the hybridization becomes more and more prominent.

E. Energy spectra vs. chain length

When the gap is large the coherence length is short and the MZMs are well localised to the ends of the chain. Correspondingly, they are fixed to zero-energy (Supplementary Fig. 11 a). When the gap is small, the coherence length is long and the MZMs hybridize, leading to the oscillatory pattern of the low-energy LDOS along the chain. Correspondingly, they split in energy and also oscillate as a function of chain length (Supplementary Fig. 11 b,c) [2, 3]. By comparison with the experimental Fig. 4 b in the main text, we can safely conclude that the experimental system corresponds to the "small gap" scenario.

F. Chain embedded in extended substrate

The results summarized in Fig. 3 of the main text are based on a four-atomic unit cell. The observed side features are concentrated at the sides of the unit cell

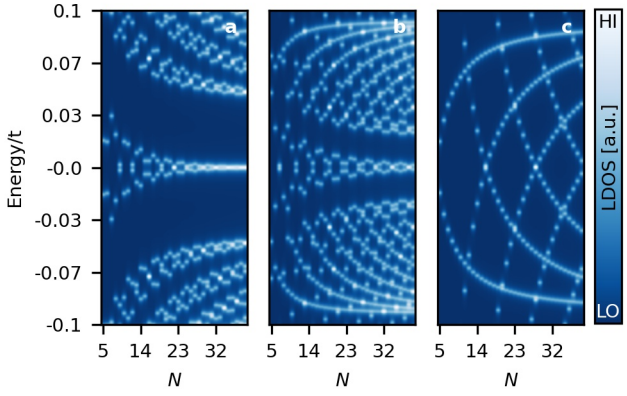

Supplementary Figure 11. **Low energy spectra vs. N for model (1) in the topologically nontrivial phase, OBC imposed.** **a,** Large gap case, $(\Delta, \alpha, \mu, J) = (0.15, 0.1, 1.35, 6)t$. The MZMs do not oscillate because the bands are well-gapped so the coherence length is short and the MZMs do not hybridize. The MZMs are local to the ends of the chain; the coherence length is $\xi = 5$. **b,** Medium gap case, $(\Delta, \alpha, \mu, J) = (0.15, 0.1, 1.4, 3.5)t$. The MZMs hybridize weakly and oscillate in energy; the coherence length is $\xi = 42$. **c,** Small gap case, $(\Delta, \alpha, \mu, J) = (0.05, 0.01, 2.05, 3.6)t$. The hybridization is strong and the MZMs also completely intersect bulk states. This example shows a remarkable similarity with the experiment (Fig. 4 b of the main text); the coherence length is $\xi = 170$.

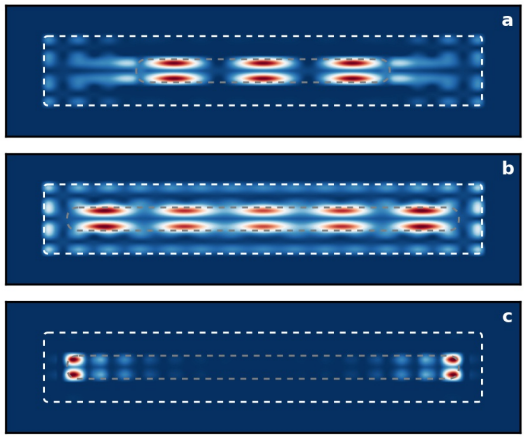

Supplementary Figure 12. **Zero-energy LDOS for the simplified model on an extended substrate.** The white dashed box indicates the size of the substrate while the grey dashed line marks the size of the chain (including the atoms next to it). **a,** $N = 33$ chain on a substrate consisting of 57×3 unit cells. The LDOS is very similar to Fig. 3 d of the main text. Parameters used $(\Delta, \alpha, \mu, J) = (0.05, 0.01, 2.05, 3.8)t$. **b,** $N = 51$ chain on a 57×3 unit cell substrate. The LDOS is very similar to Fig. 3 e of the main text. Parameters used $(\Delta, \alpha, \mu, J) = (0.05, 0.01, 2.05, 3.95)t$. **c,** $N = 51$ chain on a 57×3 unit cell substrate. The LDOS is very similar to Fig. 3 g of the main text. Parameters used $(\Delta, \alpha, \mu, J) = (0.05, 0.01, 1.35, 6)t$. OBCs are imposed in all subfigures.

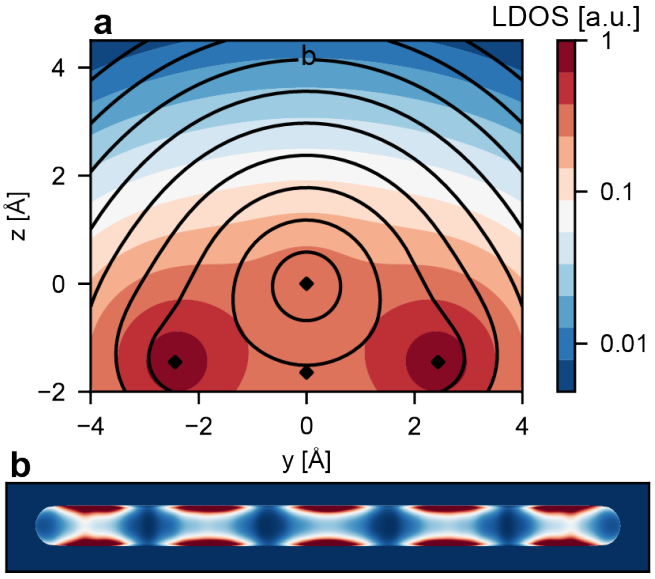

Supplementary Figure 13. **Constant-current tip trajectory and zero energy LDOS**. **a,** Cross-section through the middle of a Mn_{51} chain from Fig. 2 **c** of the main text. Constant current contours are shown as black lines. The zero energy LDOS is shown as filled color contours (log scale). Atom sites are shown as black diamonds. **b,** dI/dV map (linear scale) for the constant current setpoint labeled in **a**. Parameters: $V_{\text{stab}} = -30$ meV, $\xi = 1$ Å.

which is surrounded by hard-wall boundaries. In order to rule out confinement effects as the source of the observed side features, we have extended the simplified model, introduced in Fig. 3 of the main text and further discussed previously, and increased the substrate size. Essentially we have added more unit cells around the chain with the magnetic atom omitted. In addition, we scaled all the new hoppings by a global factor in order to slightly reduce them. As the DFT results have revealed, underneath the magnetic adatom, atomic positions are slightly contracted leading to a closer distance between the atoms. As a lowest order effect, we assume that the closer distance between two atoms results in a slightly increased hopping amplitude. It seems, hence, appropriate to slightly decrease the hoppings which are not within the unit cell that contains the magnetic atom. We have also varied the size of the substrate and considered asymmetric scenarios where the chain is not in the center but slightly off the center of the substrate. Moreover, we have studied a substrate with 3 and a half unit cells in the y-direction, but also situations with periodic boundary conditions imposed.

The results shown in Supplementary Fig. 12 summarize our analysis and essentially reproduce what is shown in Fig. 3 in the main text. There are sometimes small differences and some parameter fine tuning might be necessary, but the important finding is that side features always persist and are thus not due to confinement. These results further substantiate our previous results.

SUPPLEMENTARY NOTE 4. SIDE-FEATURES IN A CONSTANT-CURRENT FEEDBACK LOOP

In the main text, we show the LDOS evaluated in the plane of the chain. However, as explained in the Methods section, the height of the tip apex is controlled by stabilizing the tip at a bias voltage V_{stab} and current I_{stab}. To compare the theoretical LDOS to the experimental dI/dV, we follow a phenomenological description of the tunneling given in Ref. [4]:

$$\frac{dI(\boldsymbol{r}, V)}{dV} \propto \sum_i w(|\boldsymbol{r} - \boldsymbol{r}_i|) N(\boldsymbol{r}_i, eV), \tag{10}$$

$$I(\boldsymbol{r}, V) \propto \sum_i w(|\boldsymbol{r} - \boldsymbol{r}_i|) \int_0^{eV} d\omega N(\boldsymbol{r}_i, \omega), \tag{11}$$

$$w(r) = \exp\left(-r/\xi\right). \tag{12}$$

The differential conductance, $dI(\boldsymbol{r}, V)/dV$, is a weighted sum of the LDOS, $N(\boldsymbol{r}_i, eV)$, weighted by an exponential decay, $w(r)$, depending on the distance between the tip and site i and a decay length ξ. Similarly, the current, $I(\boldsymbol{r}, V)$, is a weighted sum of the integrated LDOS with the same weight.

In Supplementary Fig. 13 **a**, we show a cross section through the middle of a Mn_{51} chain with the same parameters as Fig. 2 **c** in the main text. As we follow a constant current line above a Nb site to the Mn site ($y = 2.4$ Å to $y = 0$), the zero energy LDOS goes from a large

intensity to a low intensity, resulting in a side feature. In Supplementary Fig. 13 **b**, we show an example of a dI/dV map using a constant-current feedback loop. Supplementary Fig. 13 **b** has the same side-features as Fig. 2 **c** of the main text.

SUPPLEMENTARY NOTE 5. EXTENDED SPECTROSCOPIC DATA OF SUB-GAP STATES AROUND MANGANESE AND IRON CHAINS

The experimental data in the main text only show the spatial distributions of selected states close to zero energy. In Supplementary Fig. 14, we show additional dI/dV maps measured around Mn (panels a,b) and Fe (panel c) chains at different energies. It is clearly visible that the respective lowest-energy states (at $|E| < 150\,\mu$eV) are all located on the sides of the chain, in agreement with the conclusions of the main text. In contrast, the higher-energy excitations can also be located on the chain's center as they belong to a band emerging from the hybridizing YSR states induced by a different orbital of Mn [5].

Notably, the LDOS at exactly zero energy around the two Mn chains shown in this figure is dominated by a defect-induced localized sub-gap state. The positions of the defects are marked by the green arrows in the constant-current images. At this position along the chain, a strong, near-zero energy state appears on the side of the chain. It is very likely that this state is not a property of the Mn chain itself but rather induced by the defect, which is why we chose to show the next higher energy excitation in the main text. A comparison of the datasets in Supplementary Fig. 14 with the zero-energy dI/dV map in Fig. 3 of Ref. 5 shows that the side features are typically distributed along the entire side of the chain (cf. Fig. 3 in Ref. 5 with Fig. 2 c and Fig. 3 d of the main text of the present work). Thus, it is highly likely that the zero energy states ($E = 0\,\mu$eV) localized near the defect in Supplementary Fig. 14 a,b are induced by this local perturbation. Moreover, we emphasize that the defect could possibly act as a scattering center for the interfering Bogoliubov-de-Gennes quasiparticles [5] at all energies in the chain, thereby perturbing the oscillatory pattern of the sub-gap states.

SUPPLEMENTARY NOTE 6. SUB-GAP STATES INDUCED BY IRON ATOMS AND DIMERS

Single Mn atoms on Nb(110) have recently been found to induce pairs of spatially anisotropic multi-orbital YSR states [5–7], which are oriented along the high-symmetry directions of the underlying substrate. Accordingly, the localization of sub-gap features along the sides of Mn chains on Nb(110) was explained by a band formed by the hybridization of YSR states stemming from a particular orbital featuring extended lobes along the $[1\bar{1}0]$ direction [5]. In contrast, single Fe atoms on Nb(110) only show resonances very close to the coherence peaks of Nb [7, 8] at $E \approx \pm\Delta_{\mathrm{Nb}} = \pm 1.52\,$meV, indicating that the YSR states are almost merged with the coherence peaks. These states are shown in Supplementary Fig. 15 a, b and do not feature a distinct anisotropic spatial distribution. Therefore, the side localization of the observed features in Fe chains cannot be explained just by linear combination of the YSR states of the individual constituents. However, dimers of Fe atoms [9] constructed along the [001] direction (Supplementary Fig. 15 c) do already show pronounced YSR states at lower energies, i.e., approaching E_F. But, they are still mainly located on the center of the dimer and not on the sides. Therefore, the side features around Fe chains shown in Fig. 4 c of the main text are a surprising observation not obviously related to YSR physics of the individual atoms.

SUPPLEMENTARY REFERENCES

[1] J. Li, H. Chen, I. K. Drozdov, A. Yazdani, B. A. Bernevig, and A. H. MacDonald, "Topological superconductivity induced by ferromagnetic metal chains," Phys. Rev. B **90**, 235433 (2014).

[2] T. D. Stanescu, R. M. Lutchyn, and S. Das Sarma, "Dimensional crossover in spin-orbit-coupled semiconductor nanowires with induced superconducting pairing," Phys. Rev. B **87**, 094518 (2013).

[3] L. Schneider *et al.*, "Precursors of Majorana modes and their length-dependent energy oscillations probed at both ends of atomic Shiba chains," Nat. Nanotechnol. **17**, 384–389 (2022).

[4] B. E. Feldman *et al.*, "High-resolution studies of the Majorana atomic chain platform," Nat. Phys. **13**, 286–291 (2017).

[5] L. Schneider *et al.*, "Topological Shiba bands in artificial spin chains on superconductors," Nat. Phys. **17**, 943–948 (2021).

[6] P. Beck *et al.*, "Spin-orbit coupling induced splitting of Yu-Shiba-Rusinov states in antiferromagnetic dimers," Nat. Commun. **12**, 2040 (2021).

[7] F. Küster *et al.*, "Correlating Josephson supercurrents and Shiba states in quantum spins unconventionally coupled to superconductors," Nat. Commun. **12**, 1108 (2021).

[8] A. B. Odobesko *et al.*, "Observation of tunable single-atom Yu-Shiba-Rusinov states," Phys. Rev. B **102**, 174504 (2020).

[9] F. Friedrich, R. Boshuis, M. Bode, and A. B. Odobesko, "Coupling of Yu-Shiba-Rusinov states in one-dimensional chains of fe atoms on Nb(110)," Phys. Rev. B **103**, 235437 (2021).

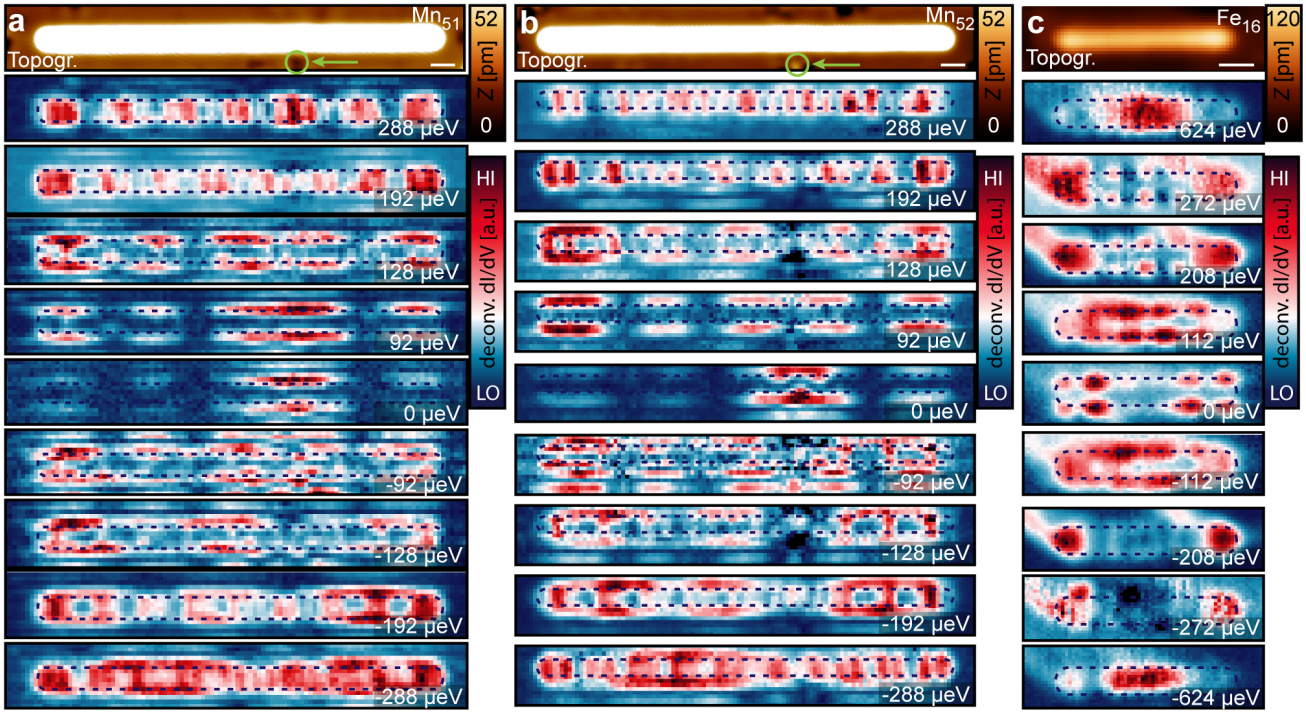

Supplementary Figure 14. **Extended spectroscopic measurements of sub-gap states around linear Mn and Fe chains. a,** Constant-current image with enhanced contrast (top panel) and deconvoluted dI/dV maps (bottom panels) at various sub-gap energies as indicated on each panel for the Mn_{51} chain presented in Fig. 4 a of the main text. The white bar corresponds to 1 nm and the green arrow highlights the position of a defect on the surface inducing additional sub-gap states. **b,** Constant-current image (top panel) with enhanced contrast and deconvoluted dI/dV maps (bottom panels) at various sub-gap energies for a Mn_{52} chain along the [001] direction. The white bar corresponds to 1 nm and the green arrow highlights the position of a defect on the surface inducing additional sub-gap states. **c,** Constant-current image (top panel) and deconvoluted dI/dV maps (bottom panels) at various sub-gap energies for the Fe_{16} chain presented in Fig. 4 c of the main text. The white bar corresponds to 1 nm. The apparent extent of the chains from the constant-current images is marked by the dark dashed lines in all dI/dV maps. Parameters: $V_{\mathrm{stab}} = -6\,\mathrm{mV}$, $I_{\mathrm{stab}} = 1\,\mathrm{nA}$, $V_{\mathrm{mod}} = 20\,\mu\mathrm{V}$.

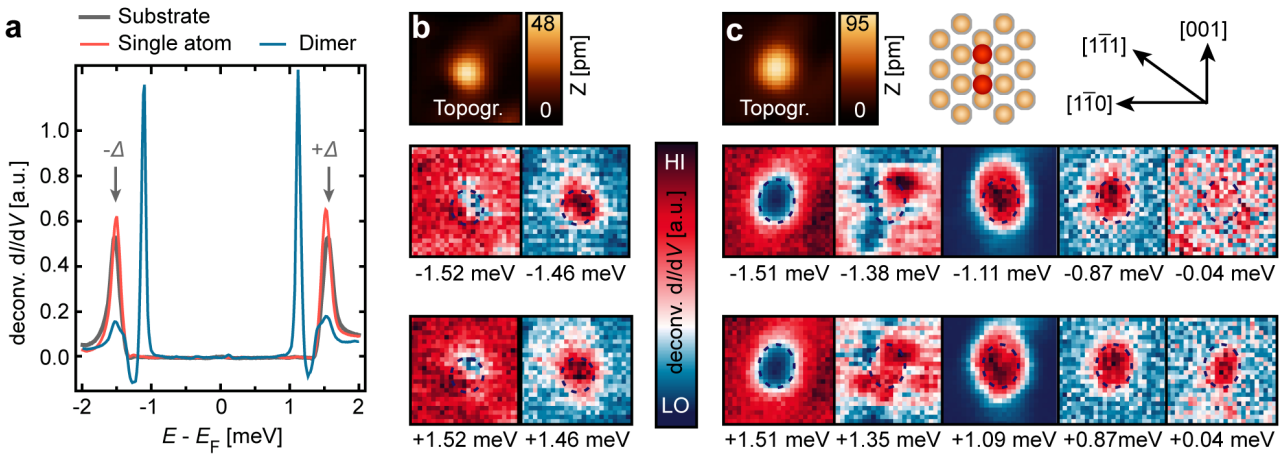

Supplementary Figure 15. **Sub-gap states induced by Fe atoms and dimers on Nb(110). a,** Deconvoluted dI/dV spectra measured on the bare Nb substrate (gray), on a single Fe atom (red) and on an Fe dimer along the [001] direction (blue). The energetic position of the Nb substrate's coherence peaks is marked by $\pm\Delta$. **b,** Constant-current image (top panel) and deconvoluted dI/dV maps (bottom panels) at sub-gap energies as indicated in the proximity of a single Fe atom (image sizes are 2 x 2 nm^2). **c,** Constant-current image (top panel) and deconvoluted dI/dV maps (bottom panels) at sub-gap energies around an Fe dimer along the [001] direction. The geometry of the dimer is sketched to the right of the constant-current image (brown spheres: Nb atoms, red spheres: Fe atoms, image sizes are 2.5 x 2.5 nm^2). The apparent extent of atom and dimer, respectively, are marked by the black dashed lines in the dI/dV maps. Parameters: $V_{\mathrm{stab}} = -6\,\mathrm{mV}$, $I_{\mathrm{stab}} = 1\,\mathrm{nA}$, $V_{\mathrm{mod}} = 20\,\mu\mathrm{V}$.